Supplement material for: A seismological large-N multisensor experiment to study the magma transfer of intracontinental volcanic fields: The example of the Eifel, Germany

T. Dahm * [1,2], **M. Isken** [1], **C. Milkereit** [1], **Ch. Sens-Schönfelder** [1], **F. Eckel** [3], **X. Yuan** [1], **M. C. Reiss** [4,8], **G. Petersen** [1], **S. Cesca** [1], **A. Oth** [7], **G. Ruempker** [8], **L. De Siena** [4,10], **P. Büyükakpinar** [1], **P. Laumann,** [1], **H. Zhang,** [1], **B. Knapmeyer-Endrun** [11,12], **S. Mikulla** [1], **R. Bauz** [1], **S. Busch** [9], **M. Hensch** [5], **B. Schmidt** [6]

[1]GFZ Helmholtz Centre for Geosciences, Potsdam, Germany, [2]Institute of Geosciences, University of Potsdam, Potsdam, Germany, [3]Kiel University, Kiel, Germany, [4]University of Mainz, Mainz, Germany , [5]LEB Freiburg, Germany , [6]Geological-Survey Mainz, Germany , [7]Luxembourg Luxembourg, Germany , [8]Frankfurt University Frankfurt, Germany , [9]Geologischer Dienst NRW, Germany , [10]Dept. of Physics and Astronomy, University of Bologna, Italy , [11]Bensberg Observatory, University of Cologne, Cologne, Germany , [12]Now at: Microgravity User Support Center, German Aerospace Center (DLR), Cologne, Germany

AutoStatsQ tests

The amplitude gain and sensor orientation tests are described in detail in Petersen et al. (2019). Here, we provide a brief overview of the methodology to aid the interpretation of the reported results of the quality tests.

Orientation of horizontal components

The test for sensor orientations is based on the polarization of Rayleigh waves. Rayleigh waves have a 90° phase shift between the vertical and the radial component seismic records. In the test, waveforms of a set of shallow, teleseismic events (M 6.0-7.8) are analyzed by rotating the horizontal traces in steps of 1°. For each rotation step, the cross-correlation of the Hilbert-transformed vertical component (Z) and the rotated radial component (Rrot) is computed. Correctly oriented sensors would result in a maximum cross-correlation value without any additional rotation compared to the theoretical radial direction. The median rotation angle of the set of different events is used to assess possible orientation errors. By using a set of azimuthally differently oriented results and reporting the median, we avoid over-interpreting single results that may be biased by crustal-scale structures that can result in a deviation of the travel path compared to the purely geometrically determined path.

Figure S.1 shows the result of the orientation test. Table 1 provides correction angles for stations with misorientations of the horizontal components that are larger than 20 degrees.

Amplitude gains

Wrong amplitude gains can result from errors in the station metadata, like missing amplification factors, or sensor problems. We compare all maximum P phase amplitudes of vertical component records of all broadband and 1-Hz

*Corresponding author: dahm@gfz.de

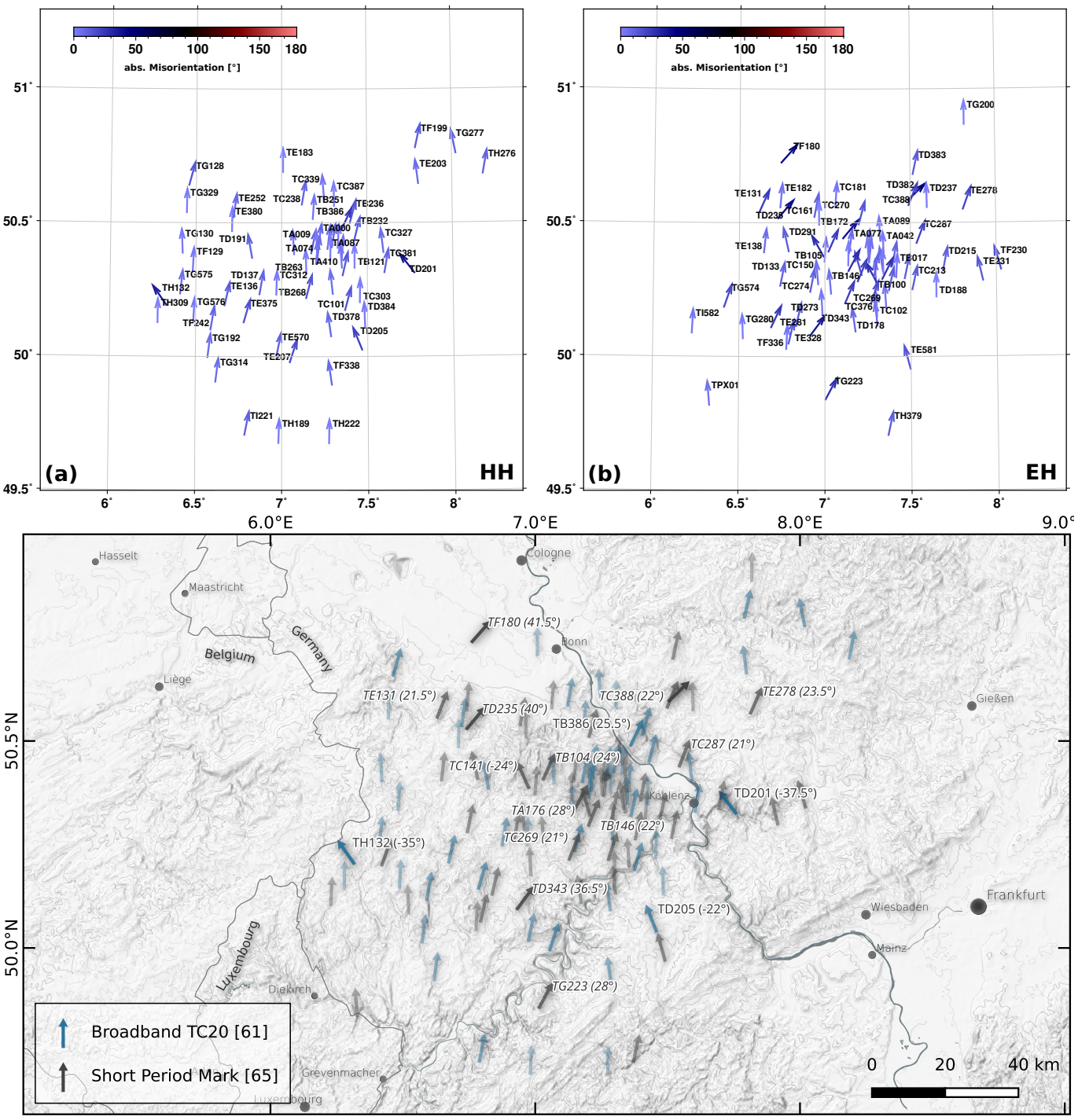

Figure S.1 Map showing the orientations of the North component as obtained from the AutoStatsQ test for short-period Mark and broadband Trillium Compact instruments. In the bottom figure the labeled locations have a misalignment of > 20 ° against north and were remapped to [EH]H[12] channel names. Regular labels denote misaligned broadband instruments, italic labels misaligned Mark instruments. Arrow opacity indicates absolute misorientations. Only stable results obtained from a minimum of five recorded teleseismic events are shown.

short-period stations to amplitudes of forward modelled synthetic data, using a global Greens's function database based on the IASPEI velocity model. We perform the test in time windows of 120 s, starting 5 s before the theoretical arrival of the first P phase. Instrument responses are deconvolved from the seismograms, and traces are filtered between 0.01 and 0.2 Hz after downsampling to 2 s. The median result of all azimuthally distributed events is considered to avoid bias from noise overlaying single events, mismatching magnitudes of single events, or travel-path effects. Smaller amplitude differences can result from site effects, while larger amplitude errors likely result from instru-

network.station	median α [°]	mean α [°]	std. dev. α [°]	N events
6E.TB386	26.0	23.2	11.1	16
6E.TD201	-38.0	-41.8	13.9	22
6E.TD205	-22.0	-26.8	13.5	11
6E.TH132	-35.0	-34.2	8.0	32
6E.TA176	28.0	29.4	10.3	8
6E.TB104	24.0	23.2	6.9	13
6E.TB146	22.0	21.1	5.5	15
6E.TC141	-24.0	-26.1	16.1	8
6E.TC269	21.0	22.6	8.9	8
6E.TC287	21.0	23.5	6.0	6
6E.TC388	23.0	24.4	7.9	11
6E.TD235	40.0	40.5	14.8	11
6E.TD343	35.0	32.9	11.6	13
6E.TD382	44.0	44.0	9.8	17
6E.TE131	21.5	21.0	9.1	6
6E.TE278	23.5	20.7	12.7	12
6E.TF180	41.0	40.6	6.3	19
6E.TG223	28.0	26.1	8.2	19

Table 1 Obtained orientation of the North component (α) for stations with $|\alpha| \geq 20°$. The horizontal line separates the Trillium Compact (20 s/120 s) broadband stations from the Mark 1 Hz sensors. For example $\alpha = 45°$ indicates that the North component points to N45E, and $\alpha = -45°$ to N45W. Note that the median angle is preferred compared to mean, as the mean angle and its standard deviation can be influenced by outliers related to structures at specific backazimuths. N *events* is the number of teleseismic event records with a sufficiently high waveform correlation that could be used for the alignment test. The here reported median values are also provided as channel azimuth in the StationXML metadata.

ment or metadata errors. We find in general a good agreement of forward modeled and observed amplitudes, with median amplitude ratio A_{obs}/A_{syn} usually below 5. Values in this order are typical for site effects, while larger values in the order of multiple magnitudes usually correspond to wrong metadata information. We manually checked all inconclusive results and conclude that the gain amplifications in the stationxml metadata of the HH and EH stations is correct.

Timing errors

The test for timing errors is based on computing cross-correlations between the recorded traces and the synthetic vertical traces in multiple-minute-long time windows starting 60 s before the first P wave and ending 600 s after the first P. In the first step for each event and station, the two vertical traces (syn. + obs.) are cross-correlated to obtain the time shift for which the correlation is highest. Only time shifts obtained from a correlation above 0.5 are considered. In the second step, the median time shift of all stations is computed for each event, and this median time shift is used to correct the time shift values at the single stations. This is done to avoid errors from wrong origin times in the catalog, to take into account large deviations between origin time and centroid time, and to consider large path effects of the teleseismic test events, which affect all of the closely located stations similarly. The test is performed in low frequency ranges (i.e., 0.02-0.10 Hz) and using synthetics computed from a global IASPEI Green's function database with a sampling of 2s (Heimann et al., 2019). Due to the low sampling rate, this test can only detect larger timing errors in the order of several seconds. We did not identify any HH or EH station with such significant timing errors.

Visualization of global seismic phases

The ground motion visualization movies were generated using a slightly adapted version of the tool provided by Ling et al. (2021), which is based on the ObsPy python-based seismology toolbox (Krischer et al., 2015). The animations consist of four main components: a ground motion map, a reference seismogram, an fk-diagram, and a ray path plot. For a detailed description of these plots, we refer the reader to the original publication (Ling et al., 2021).

In map view, the horizontal motion is depicted by the movement of the station markers S.2. The vertical up and downward motion is indicated with red-to-blue coloring. All motion is normalized station-wise. The reference seismogram in the bottom includes phase markers based on the IASP91 global seismic velocity model (Kennett and Engdahl, 1991; Snoke, 2009). To avoid many overlapping markers, P phase markers are only shown on vertical and S phase markers only on the transversal component of the seismogram. Please note that the phase markers mark theoretical arrivals estimated based on a global model, they do not provide a direct interpretation of the observed seismograms. The red line marks the time of the plot; the blue background color marks the time window used for the current fk-analysis of the vertical components waveform data. The top right polar plot shows the result of the fk-analysis in the current time window, along with the theoretical direction to the source. The polar plot shows backazimuth vs. apparent slowness [s/degrees]. The lower right plot depicts the ray path.

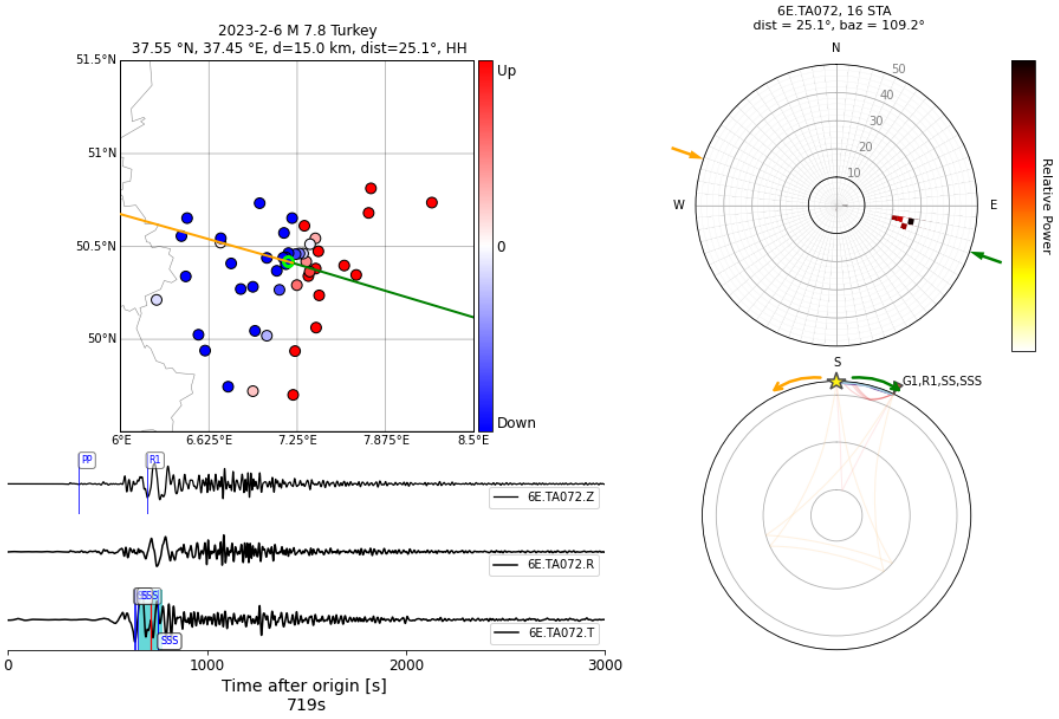

Figure S.2 Snapshot of the movie showing the Turkey 2023 earthquake (M 7.8, 2023-02-06) on broadband stations of the Eifel network. Snapshot taken 719 s after the origin time when a Love phase travels through the network. The upper left panel shows the ground motion with colors indicating polarity of the vertical component, and movement of symbols on the map depicts the motion recorded on horizontal components. The green circle marks the station for which the Z, R, and T waveforms are shown with a sliding time marker below. The green and yellow lines in the map shows the expected direction of wave arrivals as also indicated in the fk-analysis plot in the upper right and the ray path plot on the lower right. The units in the polar plot of the fk-analysis are backazimuth [degrees] vs. apparent slowness [s/degrees]

We prepared individual movies for the broadband, short-period and 4.5 Hz geophon sensors, and chose two large events: The M 7.6 Banda Sea (Indonesia) earthquake (2023-01-09) serves as an example of a teleseismic event, and

the M7.8 Turkey earthquake (2023-02-06) is an example of a regional earthquake. Thanks to the smaller distance, the latter event is also observed on the 4.5 Hz sensors, while the Banda Sea event is limited to broadband and short period sensors.

Waveform data was restituted to velocity. Ground motion is shown bandpass filtered between 0.01-0.05 Hz. The fk-analysis is performed in two frequency bands, between 0.01-0.20 Hz to emphasize body waves in 30 s sliding windows and 0.01-0.04 Hz for other phases in 120 s sliding windows.

Correlation of today uplift rates with velocity anomalies and Moho upwelling

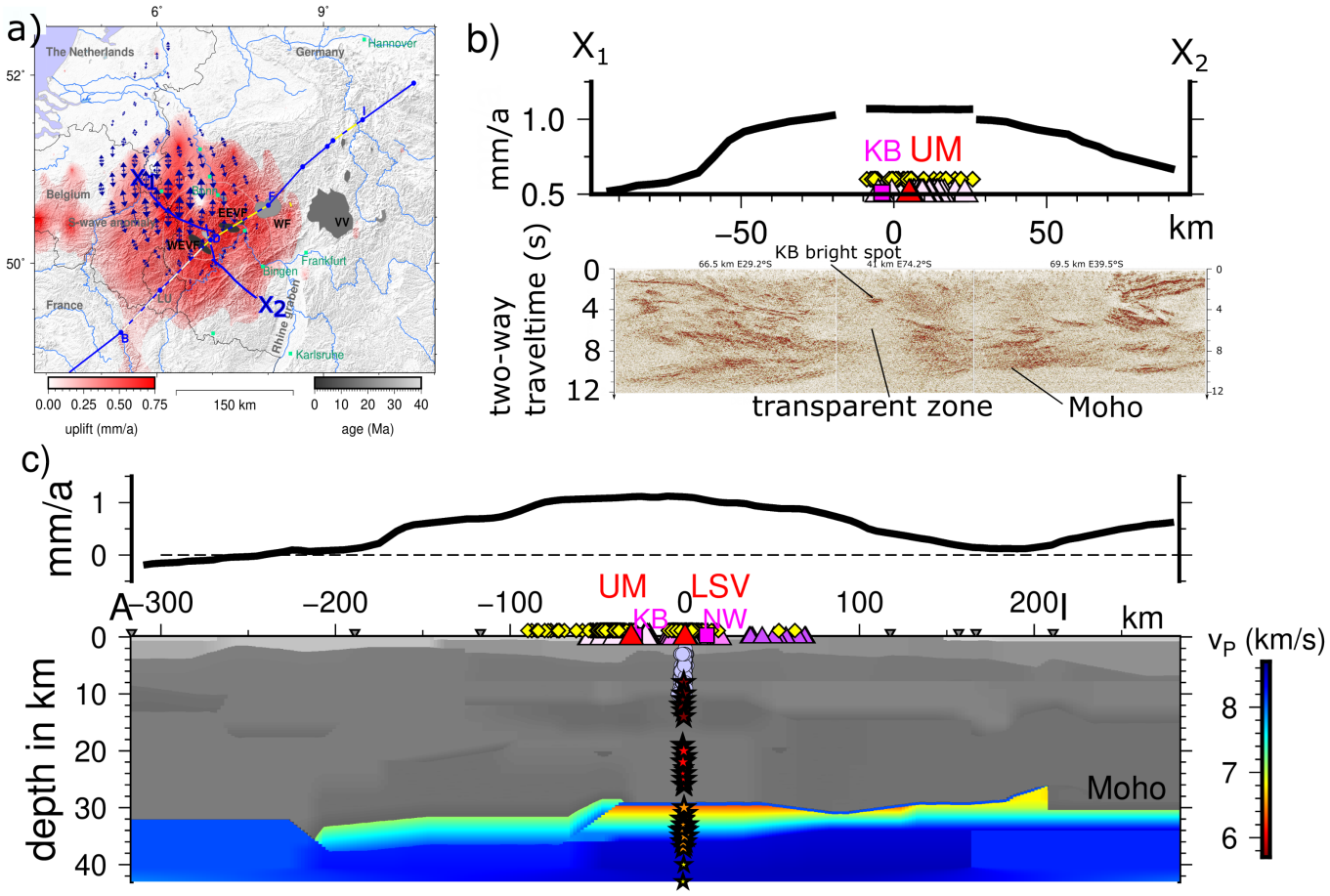

Figure S.3 Activity and structural setting of the Eifel volcanic fields. (a) Large scale uplift (gridded field) and extension rate (double arrows) derived from dense GNSS data (data from Kreemer et al., 2020). Volcanic provinces in Central Europe are indicated by grey polygons. Lines show a steep angle seismic experiment (DEKORP 1A-1C) and a wide angle refraction experiment from 1979 (both described in Dahm et al., 2020). Abbreviations are: EEVF=East Eifel Volcanic Field, WEVF=West Eifel Volcanic Field, HEVF=Hocheifel Volcanic Field, WF=Westerwald Field, VV=Vogelsberg volcano, SG=Siegener Field. UM is the youngest maar in the WEVF. LSV is the Laacher See volcano. (b) Uplift rate from the European Ground Motion Service (EGMS, e.g. Crosetto et al., 2020, 2021) are projected over the DEKORP 1 profile of the pre-stack time migration results (two-way travel time versus distance, from Dahm et al., 2020). Projected scoria cones and positions of Kelberg (KB) and Ulmener maar (UM) are indicated. (c) Vertical section of P-wave velocity derived from the refraction seismic experiment. Velocities in the upper mantle are indicated by colored field, velocities in the crust in grey scale (from Dahm et al., 2020). Deep low frequency volcanic earthquakes between 2013 and 2022 (updated from Hensch et al., 2019) are plotted by stars. Earthquake swarms beneath the volcanic centers are plotted by blue-filled circles. NW shows the projected location of the city Neuwied. The average uplift rates along the profile are indicated in the graph (data from EGMS).

SKS Splitting

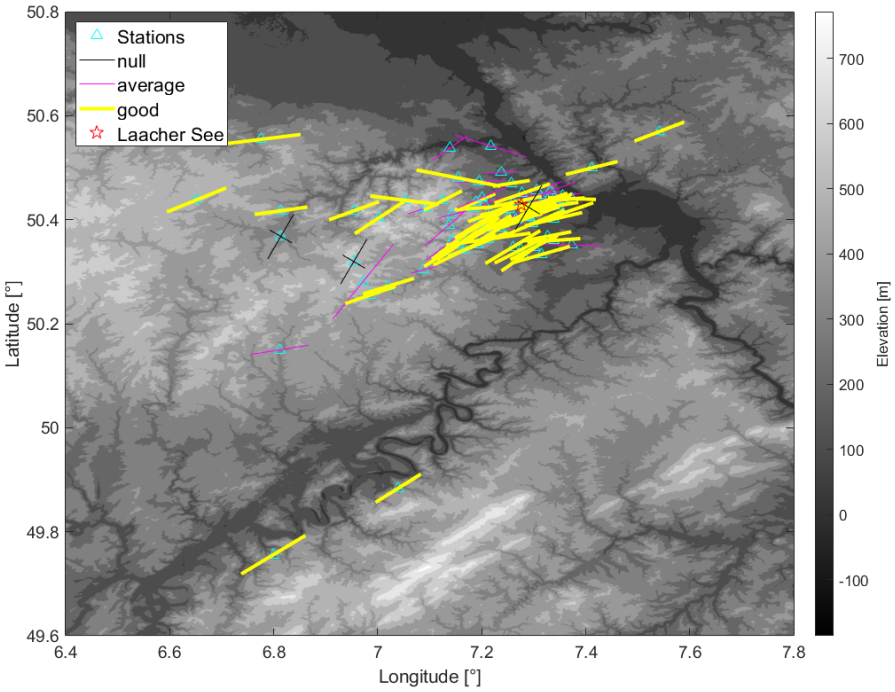

Figure S.4 Results of SKS splitting analysis of the event on 14th September 2022, 11:04 from southeast of the Loyality Islands $[-21.1909, 170.2666]$. Here, high quality and lower quality results at BB stations are plotted.

Test of different ML-pickers

We tested the performance of the different ML-pickers for the Eifel Large-N dataset, using three different architectures (PhaseNet, EQTransformer, GPD), as provided in the SeisBench package by Woollam et al. (2022). For each architecture, the weights obtained from different training datasets (original = California ; stead = global; ETHZ = Switzerland) were used. Details are provided in Woollam et al. (2022).

The tests showed that the PhaseNet model with original training data had the picks with highest confidence level and smallest residuals to manually picked P and S phases of our reference dataset (Fig. S.5). The reference dataset consisted of far more than hundreds of manual picks for both P and S phases, estimated using three component data individually for each station, including S waves that were difficult to pick (e.g., Fig. S.5a).

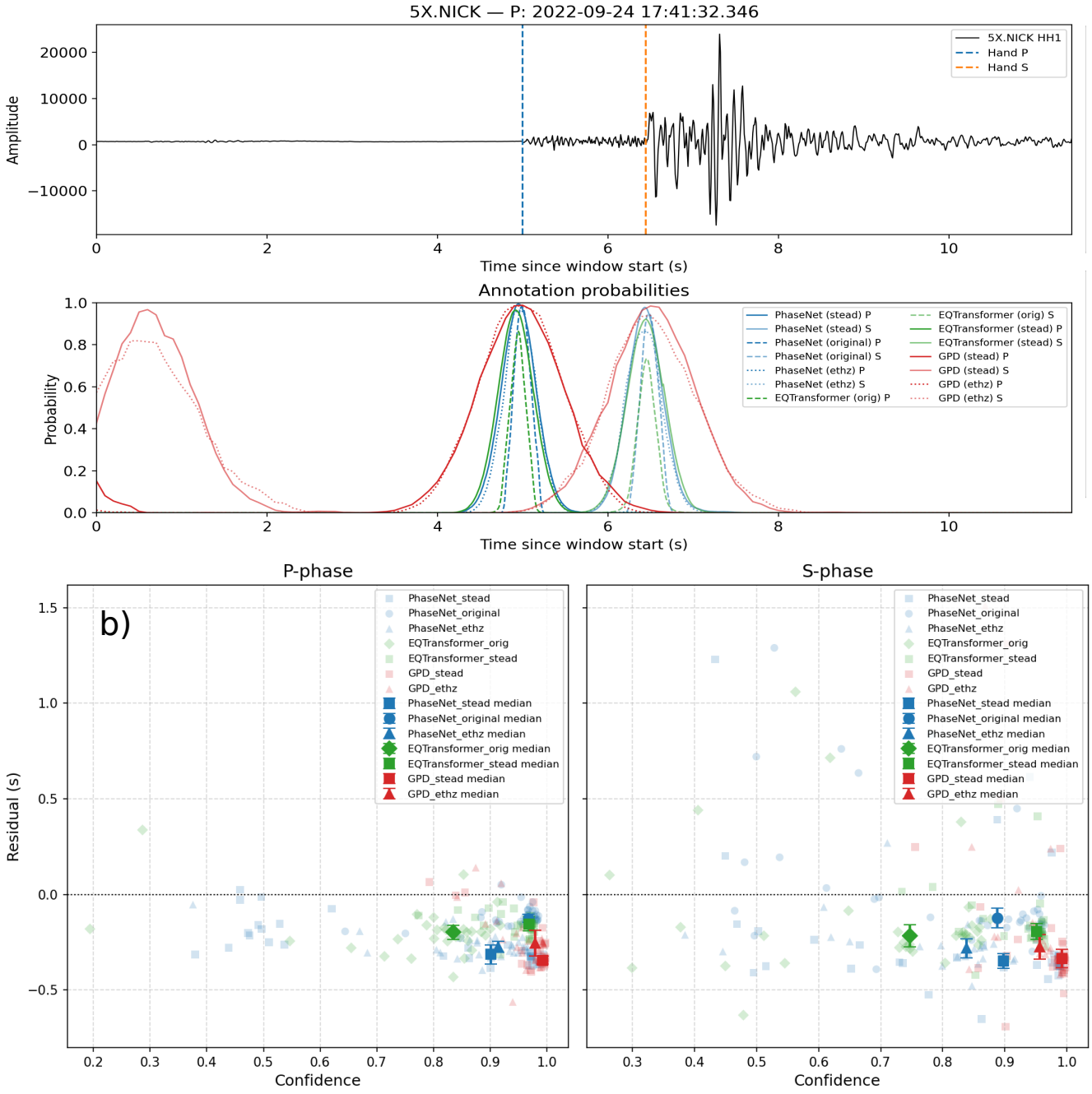

Figure S.5 Test of different ML-Phasepickers. a) Example waveform at station 5X.NICK (Z component) for a local microearthquake from 24 September 2022 Manual pick times (hand P and hand S) are indicated by dashed lines. The second subplot in a) shows the pick probability trace of three different architectures in different colours (see labels to associated different training data). b) Residuals between ML and manual picks analysed for P- and S-phases using the reference dataset. Scatter plots show individual picks (semi-transparent), while large markers with error bars indicate the median residual and the median absolute deviation (MAD) for each model. As above the colors distinguish architecture model (PhaseNet, EQTransformer, GPD), while marker shapes indicate different training datasets.

References

Heimann, S., Vasyura-Bathke, H., Sudhaus, H., Paul Isken, M., Kriegerowski, M., Steinberg, A., and Dahm, T. A Python framework for efficient use of pre-computed Green's functions in seismological and other physical forward and inverse source problems. *Solid Earth*, 10(6): 1921–1935, 2019. doi: 10.5194/se-10-1921-2019.

Kennett, B. and Engdahl, E. Traveltimes for global earthquake location and phase identification. *Geophysical Journal International*, 105(2): 429–465, 1991.

Krischer, L., Megies, T., Barsch, R., Beyreuther, M., Lecocq, T., Caudron, C., and Wassermann, J. ObsPy: A bridge for seismology into the scientific Python ecosystem. *Computational Science & Discovery*, 8(1):014003, 2015.

Ling, O. K. A., Stähler, S. C., Giardini, D., and AlpArray Working Group. Visualizing global seismic phases with AlpArray. *Seismological Society of America*, 92(6):3845–3855, 2021. doi: 10.1785/ 0220210046.

Petersen, G. M., Cesca, S., Kriegerowski, M., and the AlpArray Working Group. Automated Quality Control for Large Seismic Networks: Implementation and Application to the AlpArray Seismic Network. *Seismological Research Letters*, 90(3):1177–1190, 2019. doi: 10.1785/0220180342.

Snoke, J. A. Traveltime tables for iasp91 and ak135. *Seismological Research Letters*, 80(2):260–262, 2009.

Woollam, J., Mn̈chmeyer, J., Tilmann, F., Rietbrock, A., Lange, D., Bornstein, T., Diehl, T., Giuchi, C., Haslinger, F., Jozinović, D., Michelini, A., Saul, J., and Soto, H. SeisBench - A Toolbox for Machine Learning in Seismology. *Seismological Research Letters*, 2022. doi: 10.1785/0220210324.